PAPER • OPEN ACCESS

Enrichment of impurities seeded for exhaust control in a spherical tokamak power plant geometry

View the article online for updates and enhancements.

Enrichment of impurities seeded for exhaust control in a spherical tokamak power plant geometry

S.L. Newton[1,*] , **R.T. Osawa**[1] , **S.S. Henderson**[1] , **D.J. Moulton**[1], **O. Myatra**[1] and **V. Badicel**[1,2]

[1] United Kingdom Atomic Energy Authority, Culham Campus, Abingdon, Oxon OX14 3DB, United Kingdom of Great Britain and Northern Ireland
[2] York Plasma Institute, Department of Physics, University of York, York YO10 5DD, United Kingdom of Great Britain and Northern Ireland

E-mail: sarah.newton@ukaea.uk

CrossMark

Abstract

Through SOLPS-ITER simulations, we have investigated the ability of seeded argon and neon impurities to effectively control divertor power loading in a power-plant-class spherical tokamak geometry. We consider a connected double null equilibrium, with a well-baffled, extended outer divertor leg and a short, weakly baffled inner divertor leg. As the impurity can significantly impact fusion performance if it travels upstream to the main confined plasma, measures of the success in restricting power loads are given by the corresponding impurity compression and enrichment, quantifying the ratio of the amount of impurity found upstream to that in the divertor. In this study, we work with a fixed input power of 100 MW, constant transport coefficients, so no ballooning effects on transport are modeled and drifts are turned off, and weakly varied main ion fueling from external gas puffs. The impurity seeding is varied to produce detachment, giving radiation losses from the closed field line region up to around 10 MW. We find that argon reduces the target power loads effectively, with a high radiation efficiency, and remains well localized as the outer leg detaches. Argon compression and enrichment in the inner leg can be improved by seeding there directly, with the impurity concentration on the last closed flux surface reaching 1.5%. Neon, by comparison, is found to be a much less suitable impurity for use at this scale, with a low radiation efficiency and the impurity concentration on the last closed flux surface reaching up to 9%.

(Some figures may appear in colour only in the online journal)

---

* Author to whom any correspondence should be addressed.

1. Introduction

Power plant-class fusion facilities are expected to generate gigawatts of fusion power, and require steady-state solutions to a challenging exhaust heat management problem [1]. Assuming no radiation from the core, over 20% of the energy output from the burning toroidal plasma will exhaust through an edge 'scrape-off layer' (SOL), with current expectations [2] setting the width of such a layer to be on the order of millimeters. If unmitigated, this power will deposit on plasma facing surfaces, with no material able to withstand such a sustained power load. Diverted tokamaks use the magnetic field to split the SOL and guide it through regions which can be specially armored, the inner and outer divertor legs, to target surfaces [3].

With their compact geometry, spherical tokamaks (STs) have a particular difficulty, as the central hole through the torus is very small, so the inner divertor leg is restricted to small radii, giving a low potential 'wetted' area for power deposition. This can be ameliorated by a double null geometry, where divertor structures are introduced symmetrically at the top and bottom of the device. It is then assisted by a natural tendency for power to exhaust through the outer side of the plasma, with an in-out power balance ranging from around 1:2 in single null geometry up to around 1:10 for double-null [4–8]. The outer leg(s) can also be extended to as large a radius as is feasible, increasing the wetted area [9, 10].

The target plasma can be defined as detached when the target flux and pressure reduce as the target temperature is reduced (via increased fueling or seeding, or decreased power crossing the separatrix). It is expected that a power plant must be fully detached in steady-state operation, for example the plasma temperature is reduced below 5 eV to minimize physical target material sputtering by heavy impurity ions, and the position of the 'detachment front', a zone of strong ionization and radiation, must be well controlled [11–13].

Cooling of the divertor leg plasma can be enhanced by the seeding of impurity gases, with radiation loss curves matching the local plasma temperatures [14]. There have been extensive studies, across many devices, aimed at understanding the detailed behavior of the impurities, where [15–19] represent but a few, with, for example, the impact of seeding location, divertor shaping and baffling, and the role of flows investigated, to help develop detachment control systems [20–26]. Typical impurities seeded into the divertors of current experiments are nitrogen or neon, whereas noble gases will be required in reactor-class devices, to avoid formation of tritiated compounds, with argon expected for larger high power devices [14]. However, heavier impurities can radiate efficiently at the hotter upstream temperatures near the confined plasma. They can also ionize to high charge states if they are transported into the confined plasma, releasing many electrons and diluting the core fuel. The quality of the seeded impurity confinement in the divertor region is therefore very important and is characterized by the impurity compression and enrichment. These have been represented using various definitions in the literature, some depending on the experimental measurements available, but all representing the ratio of the seeded impurity density (for compression) or concentration (for enrichment) between the divertor and the confined plasma [27–32].

A combination of the ionization mean free path and the parallel force balance on the impurity ions, including effects of entrainment in the main plasma flow, sets how well the impurity species is confined to the divertor region [25]. High first ionization potential (FIP), allowing easy penetration of neutrals upstream, is thought to be responsible for weaker enrichment of neon as compared to argon, seen in current high-power experiments and simulations [29, 33, 34]. Yet, in low power discharges, if the detachment front moves closer to the confined plasma, low FIP may increase the core plasma impurity content [27]. If a divertor is well-baffled above the detachment front in a high-power device, it may be anticipated that enrichment may be less sensitive to the species and enrichment may remain high over a wide range of seeding, if the detachment front remains stable [31, 35]. However, with the parallel thermal force from the main ion temperature gradient increasing with ion charge, easily ionized species may be pushed upstream [29, 36, 37].

Using SOLPS-ITER [38, 39], we have therefore investigated the compression and enrichment of seeded argon and neon in power-plant-class connected double null diverted ST geometry, with a well-baffled, extended outer divertor leg. We find that argon remains well localized in the outer leg, with impurity compression (as opposed to main ion compression) dominating the enrichment, across the cases studied. The radiation properties of neon are not well matched to the scenario, and, whilst it displays an enrichment, the upstream concentration passes acceptable levels before the target power loads are sufficiently reduced. By comparison, the inner divertor leg was short and weakly baffled, and showed weak argon enrichment, although improvement was seen when seeding argon directly into the inner leg.

The geometry and setup of the SOLPS-ITER simulations used in this study are described in section 2, with further details given in the appendix. The resulting enrichment and radiation efficiencies of argon and neon in the simulations are compared, for the inner and outer divertor legs, in section 3. We end with a discussion in section 4.

2. High power double-null geometry and simulation setup

The configuration we focus on here is a toroidal, axisymmetric, up-down symmetric, connected double-null plasma with a well-baffled, extended outer divertor leg and a short, weakly baffled, inner divertor leg. We have modeled the system with SOLPS-ITER, using a quadrilateral mesh for the plasma with 34 cells radially and 148 poloidally (including the guard cells), and the triangular grid for the Monte-Carlo EIRENE code [40], which describes the atomic and molecular components of the system, covers the domain out to the first wall. The geometry setup is shown in figures 1(*a*) and (*b*), the inner boundary of
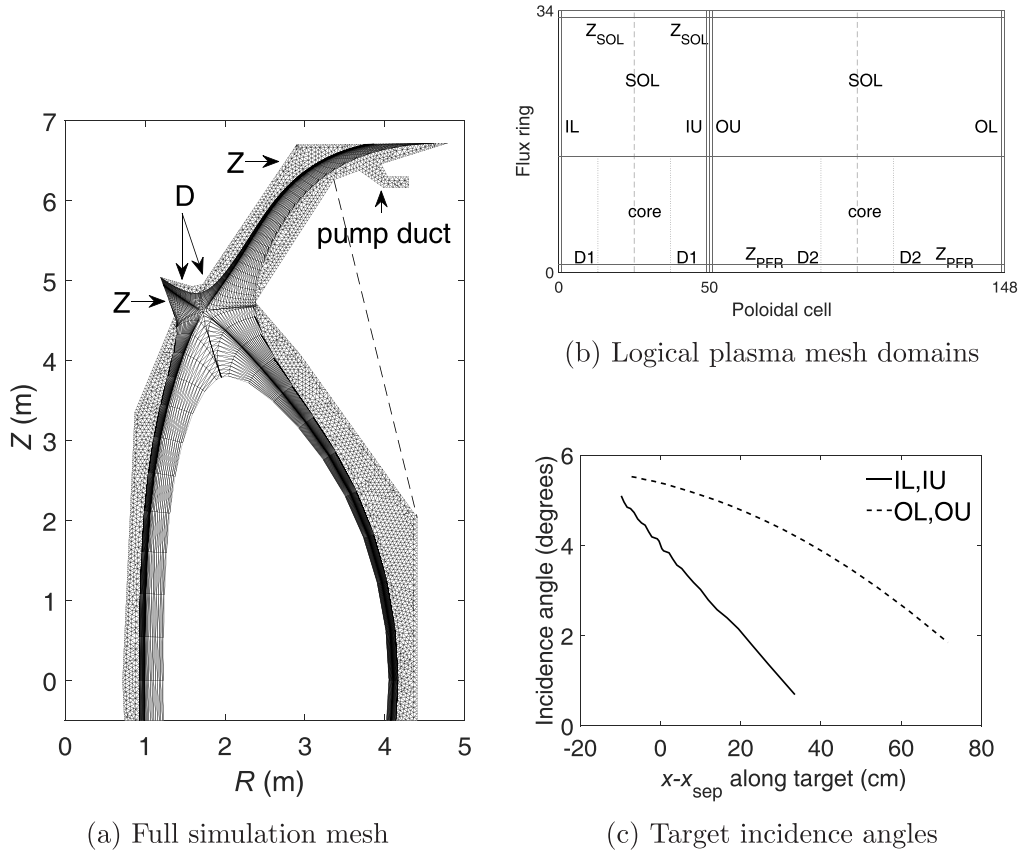
Figure 1. Simulation geometry. (*a*) Upper half of up-down symmetric connected double-null simulation mesh (quadrilateral plasma domain mesh with triangular EIRENE mesh). Deuterium (D) and impurity (Z) gas puffing locations indicated. Dashed line indicates opened wall position. (*b*) Domains on a logical representation of the plasma simulation mesh—the four unmarked regions adjacent to the core are the PFR regions. The bounding guard cell regions are marked, as are the inner lower and upper targets (IL and IU) and outer lower and upper targets (OL and OU). The plasma grid positions near the pairs of D puff valves and the PFR and SOL impurity (Z) seeding locations are labeled. (*c*) Profiles of incident magnetic field angles at the lower targets (up-down symmetric) as a function of position along the target plate with respect to the separatrix (positive in the SOL).

the simulation domain represents the interface to the main core plasma, while the last few closed flux surfaces included in the simulation domain are marked and referred to here simply as core. It can be seen that the poloidal resolution is concentrated on the divertor legs. The incidence angle of the magnetic field to the target across the plasma grid is shown in figure 1(*c*), the low values increasing the spreading of the power load over the target. This geometry is characteristic of early design phases of the STEP (Spherical Tokamak for Energy Production) program [41, 42], which aims to produce net energy from a prototype fusion energy plant in the 2040 s.

The bulk plasma is taken to consist of deuterium ions and electrons. To consider situations representative of the power plant regime, we assume 100 MW enters the simulation domain through the inner boundary, assumed to be split equally between the inner and outer surfaces and further split equally between the electrons and ions. This corresponds to around 2 GW fusion power output, with 70% radiation fraction in the main core plasma. Assuming a representative helium concentration of around 2%, then sets the D^+ ion flux into the simulation domain to 3.5×10^{22} ions s^{-1}, representing the particle outflow from the main core plasma due to pellet fueling. Note that helium was not included in these simulations. Deuterium molecules are injected, to control the SOL density, from two pairs of up-down symmetric slots near the wall below the X-points (marked with 'D' in figure 1), angled into the inner and outer divertor leg entrances. Atoms of argon or neon are seeded through an up-down symmetric pair of slots near the outer target in the wall of the private flux region (PFR), with a small number of simulations including argon seeding from an up-down symmetric pair of slots in the inner wall, just below the divertor entrance (impurity puff slots are marked with 'Z' in figure 1). Throughout, the puffed values (for impurities and deuterium) are given as the total number of atoms injected per second from each up-down pair of slots (the D puffed from the inner and outer sides was kept equal, so the total D puffed is twice the quoted value). The individual impurity charge states are followed (no bundling) and the full reaction set used in EIRENE is given in appendix A. Currents are included in the simulation while drifts were not enabled, but studies of their impact are underway [43].

Anomalous cross-field plasma transport is represented by setting anomalous transport coefficients for particles $D = 0.3$ m^2 s^{-1}, electron and ion heat $\chi = 1.0$ m^2 s^{-1} and

viscosity $\nu = 0.2$ m^2 s^{-1}. These were assumed constant throughout the domain and the same for all ion species. These values were chosen to give an outer midplane heat flux decay length of around 2 mm throughout the simulation sets, bounded by scaling expectations [2, 44]. The impact on the results presented here of profiles of these transport coefficients, for example representing a ballooning of transport at the outboard midplane [8], remains to be investigated. The electron and main ion parallel heat flux limiters (0.3 and 1.0), as well as the parallel ion viscous limiter (0.5), follow those used in [45]. These can affect the onset of detachment and up-down asymmetry in high power simulations, where particularly the ion collisionality can be low at the midplane. However, the simulations here cover a range of target conditions and we do not expect a strong impact on the trends presented. Density decay boundary conditions were used for the SOL and PFR simulation mesh edges. The wall material was taken to be tungsten, with neutral reflection properties following from the TRIM database. Pumping of both D and Ar is simulated by setting the recycling coefficient of the surface at the end of the pump ducts (up-down symmetric, see figure 1(*a*)) to $R = 0.8387$ (corresponding to a rate of 261.5 m^3 s^{-1} per pump duct), with $R = 1$ elsewhere. The angling of the duct prevents line of sight trajectories to the pumping surface. The wall temperature is taken to be 1100 K, with a reduced temperature of 580 K on the pump duct surfaces.

With the above setup, both D puff pairs at 4×10^{23} with an Ar puffing rate from the outer PFR of 6×10^{21} brings the simulation close to detachment, with reasonable Greenwald fraction. We performed an argon seeding scan around this D puffing rate, evaluating the resulting enrichment in the inner and outer divertor legs. We include a disconnected double-null simulation, with the distance between the separatrices at the outer midplane $dR_{\rm sep} = 2$ mm and an active upper X-point, with otherwise matched setup, for comparison. The inner target remained only partially detached—that is the ion temperature was high in the far SOL—due to the near-vertical geometry [46] and the fact that argon was not readily transmitted from the seeding location in the outer leg. The physical sputtering due to partial detachment, even in the far SOL, would lead to unacceptable levels of target erosion in a power plant plasma [47]. So we considered the effect of including an inner SOL argon seeding valve, which allowed full detachment of the inner divertor. A similar neon seeding scan indicated it is a much less suitable impurity for use at this scale. In the next section we detail the results of these studies.

3. Compression, enrichment and radiation efficiency

In this study we define the compression of a species as follows. The volume average of a quantity Q, over a given region $\mathcal{R}$, is defined as that quantity in a given plasma grid cell multiplied by the volume of the cell $\mathcal{V}$, summed over all cells in the region, divided by the sum of the cell volumes in that region:

$\langle Q \rangle_{\mathcal{R}} = \sum_{\mathcal{R}} Q\mathcal{V} / \sum_{\mathcal{R}} \mathcal{V}$. The 'divertor SOL' region refers to the SOL flux rings from X-point to target, $\mathcal{R} = {\rm div}$, and the 'LCFS' is taken to refer to the last closed flux ring of the core, $\mathcal{R} = {\rm LCFS}$. The compression of species s is given by the volume average over the divertor SOL of twice the molecular density n_{sm} (when present) plus the total atomic n_{s0} and ionized state density $\sum_z n_{sz}$, divided by the average of the same quantity taken over the LCFS,

$$\mathcal{C}_s = \left\langle 2n_{sm} + n_{s0} + \sum_z n_{sz} \right\rangle_{\rm div} \Bigg/ \left\langle 2n_{sm} + n_{s0} + \sum_z n_{sz} \right\rangle_{\rm LCFS}. \tag{1}$$

We note that the inclusion of the neutral and molecular density in the average over the LCFS when evaluating the main ion compression has negligible impact here. We also evaluated the compression in the inboard (outboard) divertors by replacing the denominator average over the LCFS with the average over the eight cells centered on the inboard (outboard) midplane, to highlight effects of in-out asymmetry. The trends were unchanged, with the absolute values of impurity compression roughly halved.

For the simulations considered, the compression in the divertor legs is found to be quite up-down symmetric (see discussion in appendix B). Therefore, in the rest of this paper, unless noted otherwise, for inner/outer compression we use the value averaged over the upper and lower inner/outer divertor legs. Finally the impurity enrichment is then defined as the ratio of the impurity compression to that of the main ions, $\mathcal{E} = \mathcal{C}_{\rm impurity} / \mathcal{C}_{\rm D}$. Alternative formulations which appear in literature, for example [27–29], are typically driven by the available experimental data. Using these definitions we find the same trends, although the absolute values vary. At acceptable core parameters, higher values of impurity compression will tend to indicate reduced contamination of the main core plasma and higher divertor impurity radiation, while higher impurity enrichment will tend to indicate impurities can be pumped efficiently [27].

The total D gas puff is typically an order of magnitude larger than the impurity puff across these simulations, so the pump pressure varies only weakly across the set, and is around 6 Pa. The results are presented as a function of the injected gas puff ratio, including the D$^+$ flux into the simulation core: gas puff ratio = puffed impurity flux / (puffed impurity flux + puffed D flux + core D$^+$ flux).

3.1. Argon seeding

The base set of argon seeded simulations have both D gas puffs in the small range $3 - 4 \times 10^{23}$ and Ar puff from the outer target PFR in the range $3 \times 10^{18} - 1 \times 10^{22}$, giving target power loads ranging from near unmitigated to acceptable. Across this set of simulations the inner and outer separatrix mid-plane electron densities were around 5×10^{19} m^{-3} and 4×10^{19} m^{-3}, corresponding to 0.23 and 0.18 times the Greenwald density, while the target particle fluxes had not rolled over, with peak target electron density values, inner and outer, around 1×10^{21} m^{-3}. The impurity concentration
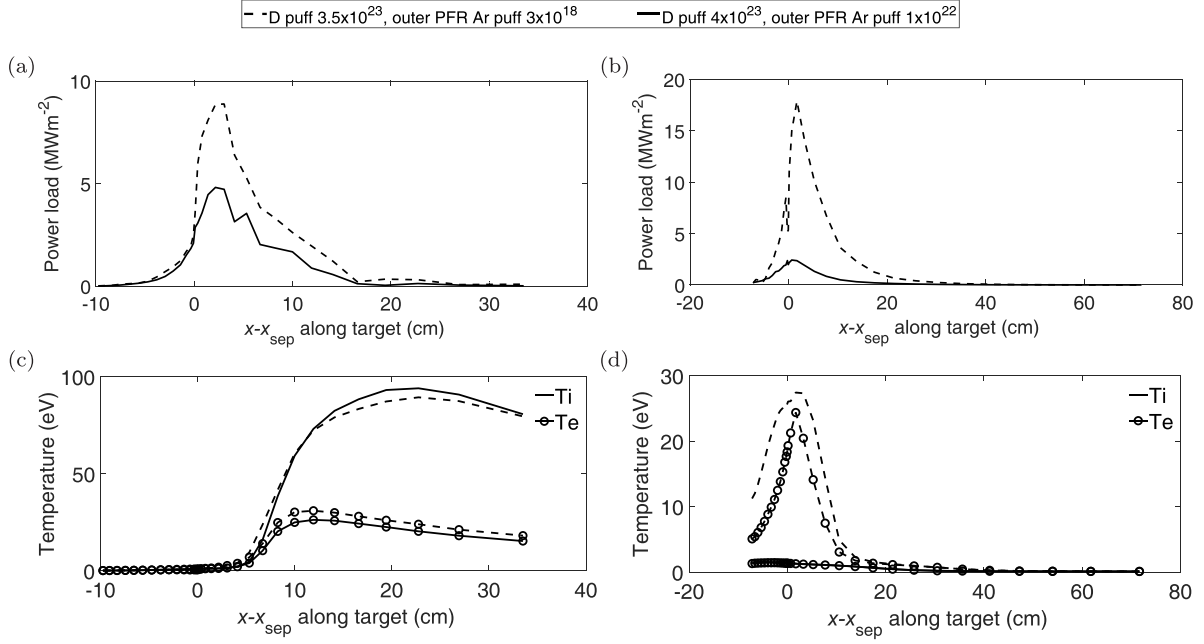
Figure 2. Range over the argon seeding scan of lower inner (left column) and outer (right column) target power load (top row) and ion (solid) and electron (circles) temperature (bottom row) profiles, as a function of position along the target plate with respect to the separatrix (positive in the SOL). Dashed line: each D puff 3.5×10^{23}, Ar puff 3×10^{18} and solid line: each D puff 4×10^{23}, Ar puff 1×10^{22}.

on the last closed flux surface was below 1%, and the effective core charge, $\left\langle \sum_j Z_j^2 n_j / n_e \right\rangle_{\text{core}}$, where the index j runs over all ion states with charge Z_j and the core average is taken over the closed field line region, is in the range 1.5–3.5. Around these upper values, performance of the main core plasma will begin to be affected, and more detailed modelling of the transport processes on the closed field lines will be required. Summed over the whole plasma mesh, the total impurity radiation reaches around 55 MW, higher by a factor of around five than that due to the deuterium.

The outer target temperatures fall to 5 eV or below, as demonstrated in figure 2, which shows the range of lower target power fluxes, consisting of the particle, neutral and surface recombination loads, and temperature profiles covered in the scan (the ranges for the upper targets are the same). The region of strong ionization and low temperature in the outer leg stays close to the target, and the radiation is seen to be distributed over the leg, it does not concentrate at the X-point. The inner divertor remains partially detached, as the far SOL ion temperature remains high as can be seen in figure 2(*c*), which would not be sustainable for steady state operation. The power crossing the outer separatrix falls steadily by around 10 MW over the scan, with a similar increase in the core impurity radiation. There is a similar reduction in the power entering the outer divertors, while the total radiation from the outer divertors increases by around 30 MW over the scan, giving a maximum around 45 MW, and reaching around 40 MW at a gas puff ratio ∼0.004. The power entering the inner divertors drops by around 3.5 MW over the scan, with around 1 MW in total radiated from the inner divertors at the lowest seeding

level, and ranging from around 3.5 MW up to 5 MW through the rest of the scan.

In figure 3 we show the compression of argon and deuterium, as well as the enrichment of argon, as a function of gas puff ratio. The inner divertor is shown on the left panel, and the outer on the right. Results with only the outer PFR Ar puff are shown as circles (configurations indicated with other marker styles are discussed successively in this section). The deuterium compression does not vary strongly over the scan, for either divertor. The trends in argon enrichment therefore follow the argon compression. The outer divertor enrichment steadily increases with gas puff ratio, with some indication of saturation at the maximum gas puff ratio considered here [27, 31]. This trend suggests that there may be enough flexibility to handle the higher outboard power load expected when ballooned transport is accounted for, but that remains to be studied in detail. There is negligible enrichment in the inner target. We note that the impurity content in the inner target remained low, as it was not transmitted well to the inner divertor from the outer PFR puff (an effect which has been seen experimentally [37]).

The result for the disconnected double null case, with active upper X-point, which had both D puffs 3×10^{23} and Ar puff 8×10^{21}, giving a gas puff ratio 0.0124, is also shown in figure 3. The simulation shows up-down asymmetry, with argon accumulating outside the secondary separatrix as the puff is in the outer PFR, which increases the apparent lower outer divertor argon compression, displayed as a downward triangle (without up-down averaging). The upper outer divertor compression and enrichment, displayed as an upward triangle (without up-down averaging), follow the trend of the
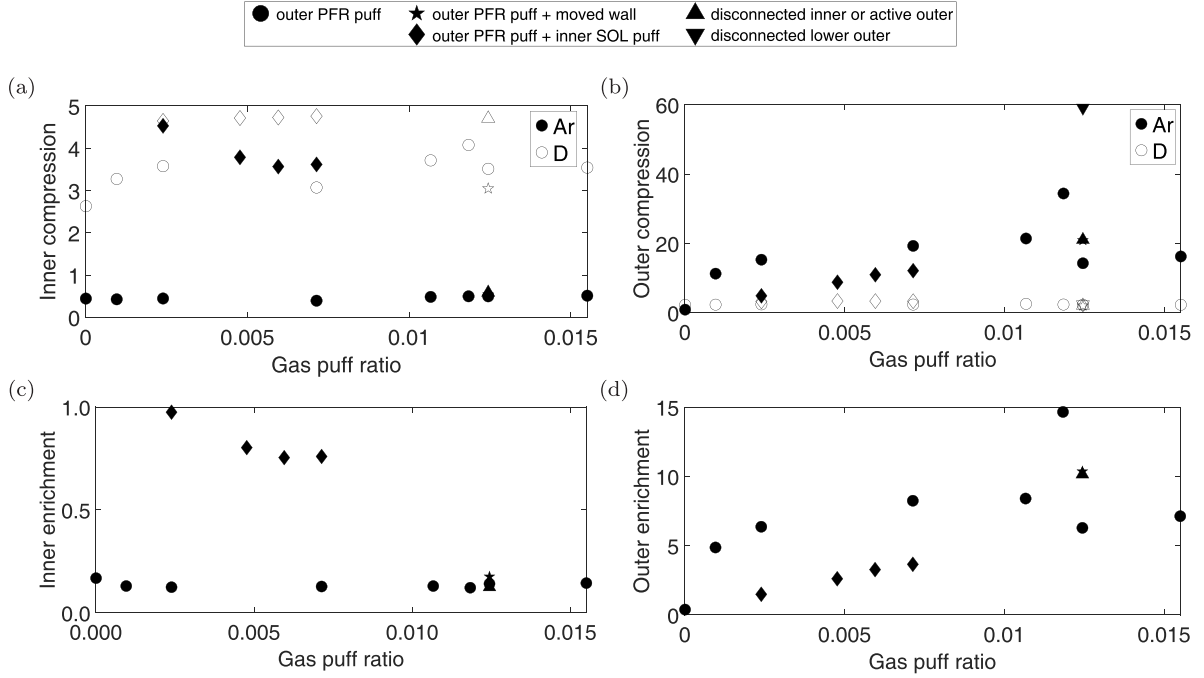
Figure 3. (Top) Argon (solid markers) and deuterium (open markers) compression and (lower) argon enrichment as a function of gas puff ratio for lower inner (left) and outer (right) divertor legs. Cases with only outer PFR Ar puff are shown as circles, pentagram marks opened outer wall case, cases with both inner and outer Ar puff are shown as diamonds. Disconnected double null case marked with upward triangle for inner divertor and the active upper outer divertor, and with a downward triangle for the lower outer divertor.

connected double null cases. The inner divertor does not have this strong asymmetry, and up-down averaged inner compression and enrichment results are shown throughout as an upward triangle for this case.

Finally we considered a connected case, again with both D puffs 3×10^{23} and outer PFR puff Ar puff 8×10^{21} so a gas puff ratio 0.0124, but with the opened outer main wall shown by the dashed line in figure 1(*a*). The target power loads are essentially unchanged, the inner target neutral pressure decreased and the ion temperature increased slightly, but the outer target neutral pressure and temperatures were also essentially unchanged. The compression and enrichment results are shown as pentagrams in figure 3 and we see they follow the main trend. The region of strong ionization in the outer leg is very close to the target, and the wall is opened above the pump duct, which may explain the lack of sensitivity. We may expect an effect on enrichment of such a change in the main wall if the detachment front were to move high up the divertor leg.

Compression is often discussed in terms of the parallel force balance on the impurities at their ionization location [25, 48]. Friction with flowing bulk ions can drag impurities, whilst the parallel bulk ion temperature gradient typically pushes them away from cool regions, such as the targets. In figures 4(*a*) and (*b*) the bulk ion parallel flow field is given for the connected and disconnected cases at matched gas puff values. Positive parallel flow is taken from the lower inner target to the outer lower target, in the direction of increasing poloidal cell number. The logical mesh representation (figure 1(*b*)) is

used to show the flow pattern clearly. The stagnation points, connected in white, highlight the up-down symmetry of the connected double-null geometry, and the ionization contours of $Ar \rightarrow Ar^{1+}$ are overlaid in black. The flow fields are similar for both cases, despite the difference in geometry—at both the inner and outer targets there is a strong upstream flow of the main ions just outside the separatrix, which encounters a downstream flow towards the X-point region coming from the midplane stagnation points. At the inner targets there is a strong ion flow in the far SOL (where there is a high ion temperature) up towards the midplane, while at the outer targets there is an ion flow up through the PFR towards the X-point. The parallel flow field of Ar^{1+} is also shown for the connected double-null case in figure 4(*c*), and is again similar in the disconnected case, and also similar for each charge state. Note the lower magnitude compared to the bulk ion flow. The inner divertor impurity flow pattern resembles that of the bulk ion flow, except for a near stagnant region in the very far SOL. The outer divertor shows a stronger flow pattern around the Ar puff locations and upstream flows around the Ar^{1+} ionization location in the PFR and SOLs. In the outer divertor legs, we find that the friction due to the flow difference with the main ions dominates the force on the Ar^{1+} around its ionization location. In figure 4(*d*) we show this force, masked by the region where the density of Ar^{1+} is $> 1 \times 10^{15}\,\mathrm{m^{-3}}$. In the outer leg the impurity is thus pushed upstream from its ionization location. In the inner leg, ionization and interactions with neutrals, which peak away from the separatrix, contribute as strongly as the friction, which peaks near the separatrix, but
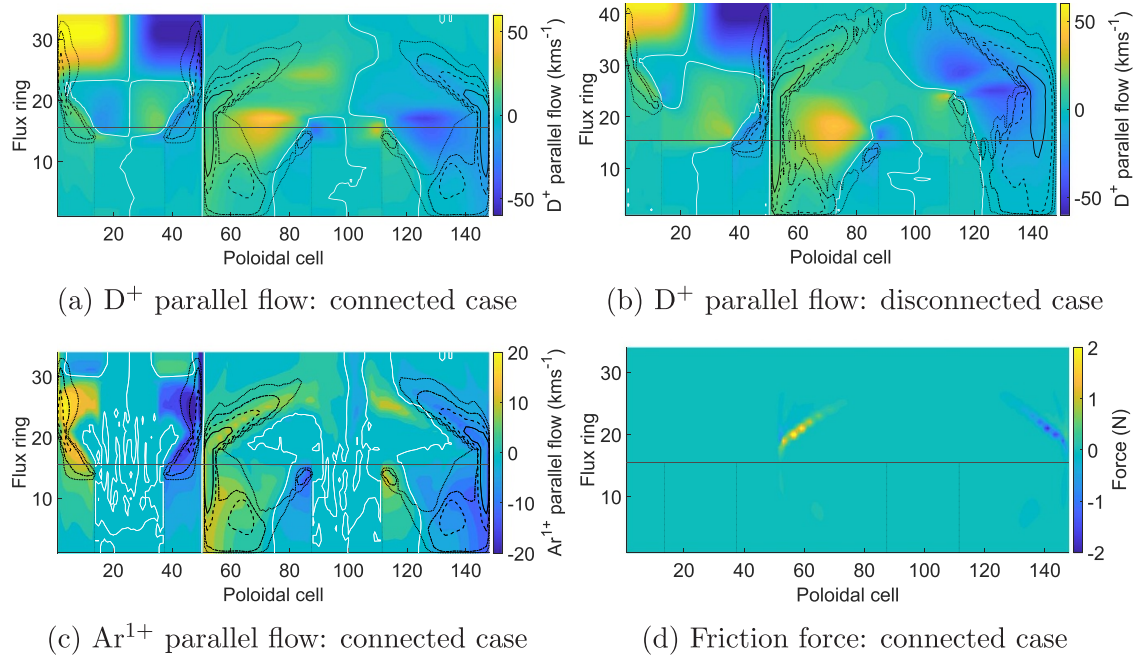
(a) D$^+$ parallel flow: connected case

(b) D$^+$ parallel flow: disconnected case

(c) Ar^{1+} parallel flow: connected case

(d) Friction force: connected case

Figure 4. Top row: Bulk ion parallel flow field on the logical representation of the plasma simulation domain, for cases with both D puffs 3×10^{23}, only outer PFR Ar puff at 8×10^{21}, for (*a*) connected double null and (*b*) disconnected double null with $dR_{\text{sep}} = 2$ mm. Lower row, for connected double null case: (*c*) Ar^{1+} parallel flow field and (*d*) parallel force due to friction against the main ion flow, masked by the region where the density of Ar^{1+} is $> 1 \times 10^{15}$ m^{-3}. White contour links bulk ion stagnation locations, black contours show ionization levels of Ar $\rightarrow$ Ar^{1+} of [1×10^{20} (dotted), 1×10^{21} (dot-dashed), 1×10^{22} (dashed), 1×10^{23} (solid)] particles s^{-1} m^{-3}. Separatrix (horizontal solid) and X-point cuts (vertical dotted) also shown.

the net impurity population is low and the individual contributions to the parallel force are negligible by comparison to the outer leg. Upstream we find peaked impurity density profiles arise in the SOL, and weak radially inward fluxes of states around Ar^{7+}, see figure 5, lead to the final upstream impurity distribution [49].

To overcome the issue of the partial inner target detachment, an inner divertor SOL Ar puff pair was introduced, marked in figure 1(*a*). An initial case with both D puffs at 4×10^{23} and both Ar puffs set to 1×10^{21} reduced the inner target ion temperature below 5 eV, and whilst the outer target power loads were acceptable at around 10 MW m^{-2}, the outer target ion temperature peaked around 15 eV. The outer Ar puff was increased, up to a gas puff ratio of 0.0071, at which both targets were close to detached (maximum outer target ion temperature around 7 eV). The power load and temperature profiles can be seen in figure 6. For comparison, we include in figure 6 the target power and temperature profiles for the case with only the outer argon puff at a matching gas puff ratio of 0.0071 (both D puffs 4×10^{23}, Ar puff 6×10^{21}), which has an impurity concentration on the last closed flux surface of 0.5%. The case with both inner and outer Ar puff is closer to detachment, but the impurity concentration on the last closed flux surface increases from 1.0% to 1.5% through that scan, which is potentially high enough to compromise good performance of the main core plasma, and creates the decrease in inner divertor compression. Increasing the outer gas puff beyond 5×10^{21} gave a weak bifurcation in the inner solution

depending on the starting simulation state—the upper inner ion target temperature continued to fall with increasing argon puff, while the lower inner target value can jump to a partially detached profile, with a maximum around 25 eV. Due to the high core impurity concentration we do not analyze these higher puff cases further here, though we note that the enrichment in either state continued to follow the trend discussed below.

The core impurity radiation was around 10 MW higher at a given gas puff ratio with both inner and outer Ar puffs, compared to the cases with only the outer PFR puff, with a similar reduction in the power crossing the outer separatrix and entering the outer divertors, while the power radiated from the inner divertor increases. The parallel flow distributions and entrainment behavior follow the same pattern as the case with only the outer Ar puff, with a reduction in the parallel flows in the inner SOL where the argon is puffed. An example of the bulk ion and Ar^{1+} parallel flow distributions, with the Ar ionization contours overlaid, is shown in figure 7, for comparison with figure 4. The additional ionization from the inner leg seeding can be seen. The ion-ion friction now dominates in the inner leg and has a broad profile, pushing Ar^{1+} in both parallel directions away from the ionization location outside the separatrix, and removing the far SOL stagnation point of the argon flow leaving a weak force directed towards the midplane. The net parallel force on the Ar^{1+} in the inner leg is a few times larger than in the case with only an outer Ar puff, but the magnitude remains less than 0.1 N, so still small compared to that
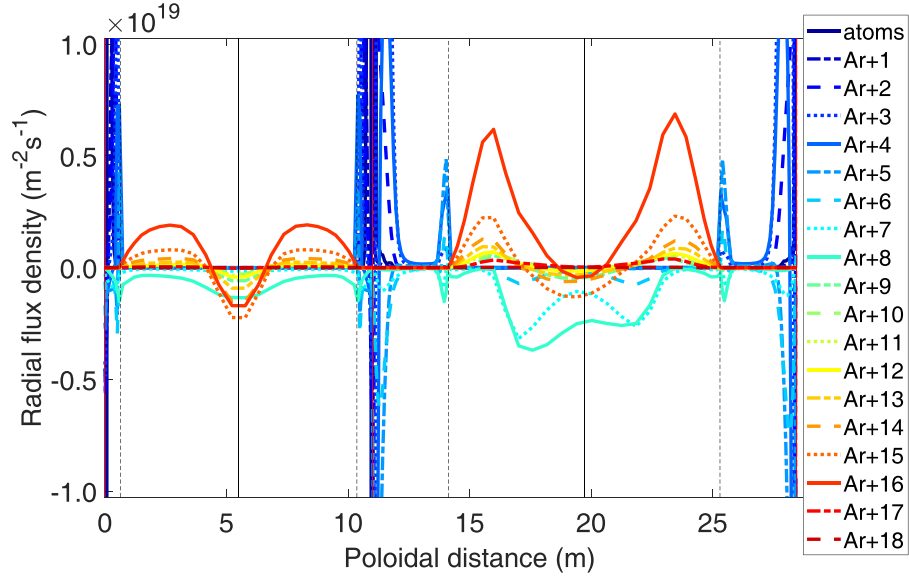
Figure 5. Radial fluxes of Ar charge states across the separatrix, negative inwards, as a function of poloidal distance along the separatrix from the lower inner target (0 m). Vertical solid line show targets and midplanes, vertical dashed lines show X-point locations. The case is connected double null with both D puffs 3×10^{23} and only outer PFR Ar puff at 8×10^{21}.
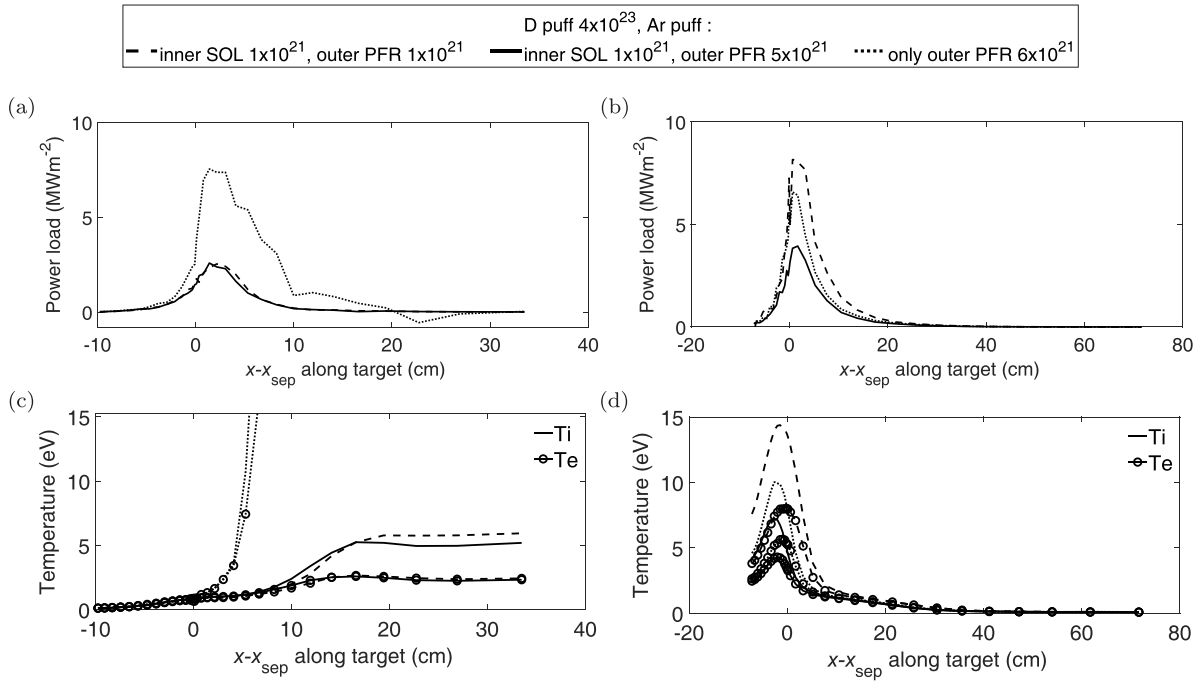

Figure 6. Range over the argon seeding scan, with both outer PFR and inner SOL Ar puffs, of lower inner (left column) and outer (right column) target power load (top row) and ion (solid) and electron (circles) temperature (bottom row) profiles, as a function of position along the target plate with respect to the separatrix (positive in the SOL). Each D puff 4×10^{23}, inner Ar puff 1×10^{21}, outer PFR Ar puff (dashed) 1×10^{21} and (solid) 5×10^{21}. For comparison, profiles (dotted) for the case with only outer PFR Ar puff, at D puffs 4×10^{23} with Ar puff 6×10^{21}, are shown.

on the impurities in the outer divertor leg. In figure 8 we show the difference in the total charged argon density distributions between the case with inner SOL Ar puff 1×10^{21} and outer Ar puff of 5×10^{21} (flow patterns in figure 7) and the case with only the outer Ar puff of 6×10^{21}, at D puffs of 4×10^{23}. We can see the effect of the inner target seeding and the increase in impurity density it produces in the core.

The compression and enrichment was evaluated for the scan, and the results are shown by diamonds in figure 3. We see that the outer divertor enrichment follows the same trend as seen with only the outer PFR Ar puff, even with the significant change in the inner divertor condition. The impurity radiation from the outer divertor also follows the same trend with gas puff ratio. The inner target enrichment was strongly increased,
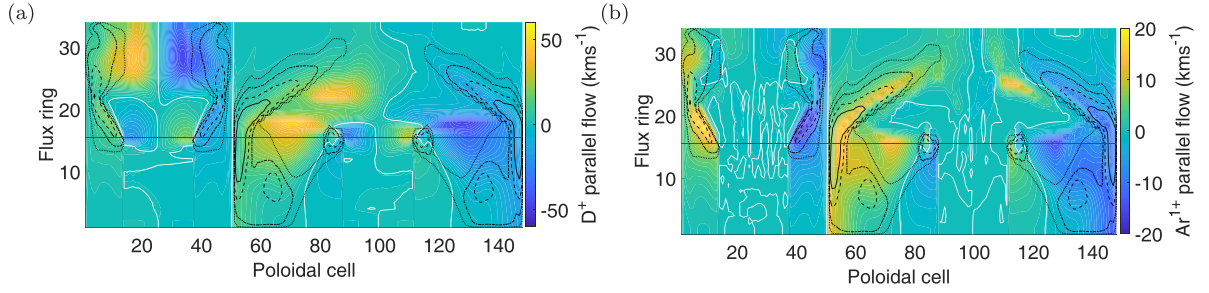
Figure 7. (Left) Bulk ion and (right) Ar^{1+} parallel flow fields on the logical representation of the plasma simulation domain, for the case with inner SOL Ar puff 1×10^{21} and outer PFR puff 5×10^{21}, with both D puffs 4×10^{23}, in connected double null. White contour identifies parallel flow stagnation location, black contours show ionization levels of $Ar \rightarrow Ar^{1+}$ of [1×10^{20} (dotted), 1×10^{21} (dot-dashed), 1×10^{22} (dashed), 1×10^{23} (solid)] particles $s^{-1} m^{-3}$. Separatrix (horizontal solid) and X-point cuts (vertical dotted) also shown.
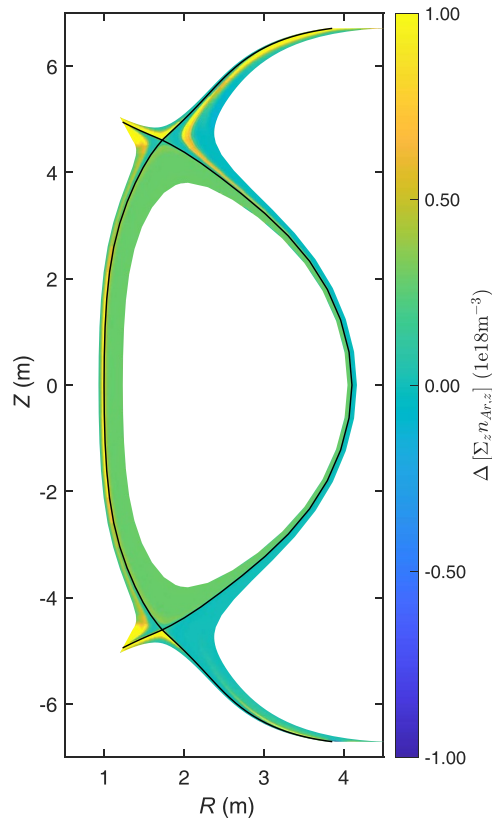

Figure 8. Difference in total ionized argon density distributions between case with inner SOL Ar puff 1×10^{21} and outer Ar puff of 5×10^{21} (flow patterns in figure 7) and the case with only the outer Ar puff of 6×10^{21}, at D puffs of 4×10^{23}. Black line indicates the separatrix.

and suggests that a lower level of inner Ar puff could be effective. This motivates future optimization of the system, including the ratio of inner to outer Ar gas puff values, fueling locations [49] and pumping, to determine possible improved divertor solutions for this geometry [50] respecting gas throughput limitations and core impurity concentrations.

3.2. Neon seeding

We now consider the enrichment in a similar base set of neon seeded simulations, in the connected double-null geometry, with seeding from the outer PFR puff only. This covered a slightly wider range in D puff $2.5 - 6 \times 10^{23}$, with the Ne puff in the range $3 \times 10^{21} - 6 \times 10^{22}$. Across the set of simulations the inner and outer separatrix mid-plane electron densities were again around $5 \times 10^{19} m^{-3}$ and $4 \times 10^{19} m^{-3}$. The total impurity radiation ranged over 35–67 MW, with that due to deuterium ranging over 7–12 MW, and again the total radiation did not concentrate towards the X-point over the scan. The power crossing the outer separatrix falls around 5 MW over the scan, with a similar increase in the core impurity radiation. There is a reduction of around 10 MW in the power entering the outer divertor, with an increase in the impurity radiation from the outer SOL of around 5 MW, while the total radiation from the outer divertor increases by around 10 MW, giving around 44 MW. The power entering the inner divertor
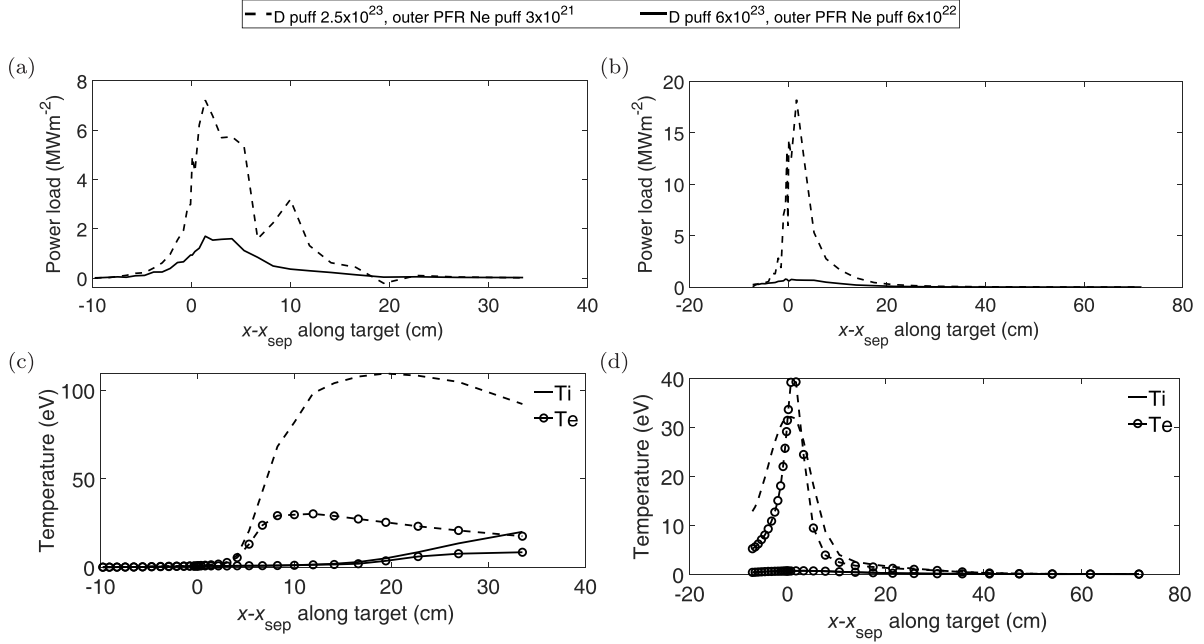
Figure 9. Range over the neon seeding scan of upper inner (left column) and outer (right column) target power load (top row) and ion (solid) and electron (circles) temperature (bottom row) profiles, as a function of position along the target plate with respect to the separatrix (positive in the SOL). Dashed line: each D puff 2.5×10^{23}, Ne puff 3×10^{21} and solid line: each D puff 6×10^{23}, Ne puff 6×10^{22}.
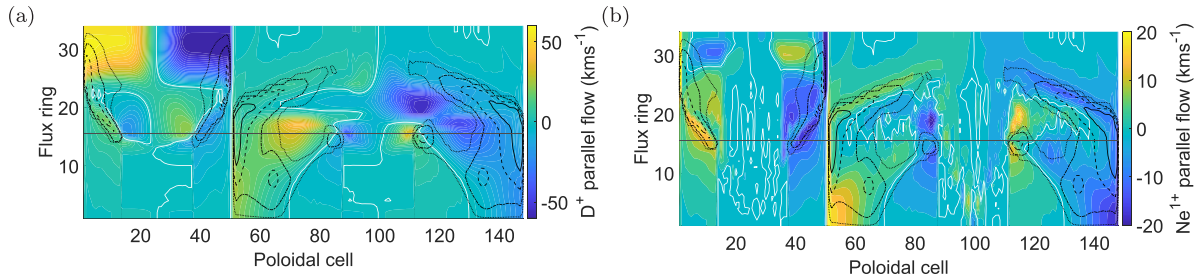

Figure 10. (Left) Bulk ion and (right) Ne^{1+} parallel flow fields on the logical representation of the plasma simulation domain, for the case with each D puff 4×10^{23}, in connected double null, with only an outer PFR Ne puff of 3×10^{21}. White contour identifies bulk ion stagnation location, black contours show ionization levels of $Ne \rightarrow Ne^{1+}$ of $[1 \times 10^{20}$ (dotted), 1×10^{21} (dot-dashed), 1×10^{22} (dashed), 1×10^{23} (solid)] particles $s^{-1} m^{-3}$. Separatrix (horizontal solid) and X-point cuts (vertical dotted) also shown.

remains roughly constant, as does the total radiation (around 10 MW) from the inner divertors.

At the very highest D and Ne puffs, the solution developed an inner up-down asymmetry, with a peak inner upper target ion temperature around 60 eV, whilst the lower inner target ion temperature peaked around 20 eV. The range of upper target power fluxes and temperature profiles covered in the scan are shown in figure 9—the power loads have only weak up-down asymmetry in the cases with lower seeding. We can see that the neon seeded scan covers a similar target profile range to the argon seeded scan. The targets steadily detach through the scan, with similar radiated power from the impurities as in the Ar seeding scan.

However, the impurity concentration on the last closed flux surface here ranges from 1.9% at the lowest gas puff ratio

(where the argon seeded value was <1%) up to nearly 9%. The FIP of neon is higher than that of argon, which is allowing the neon to penetrate upstream. This is illustrated in figure 10, where we see, by comparison to figure 7 which had a total Ar puff 6×10^{21} so gas puff ratio 0.0071, that neon penetrates the separatrix to a similar extent already at a Ne puff of only 3×10^{21}, that is a gas puff ratio 0.0036. (This argon case had lower midplane separatrix densities and power crossing the separatrix than the neon case, but this is not having a significant effect here, as the case with only an outer PFR Ar puff at 6×10^{21} had a similar flow and ionization pattern to the inner and outer Ar puff case shown in figure 7, and well matched midplane separatrix densities and powers to the neon case.) The difference in the mean free path of neutral neon and argon between these cases is illustrated in figure 11—the neon
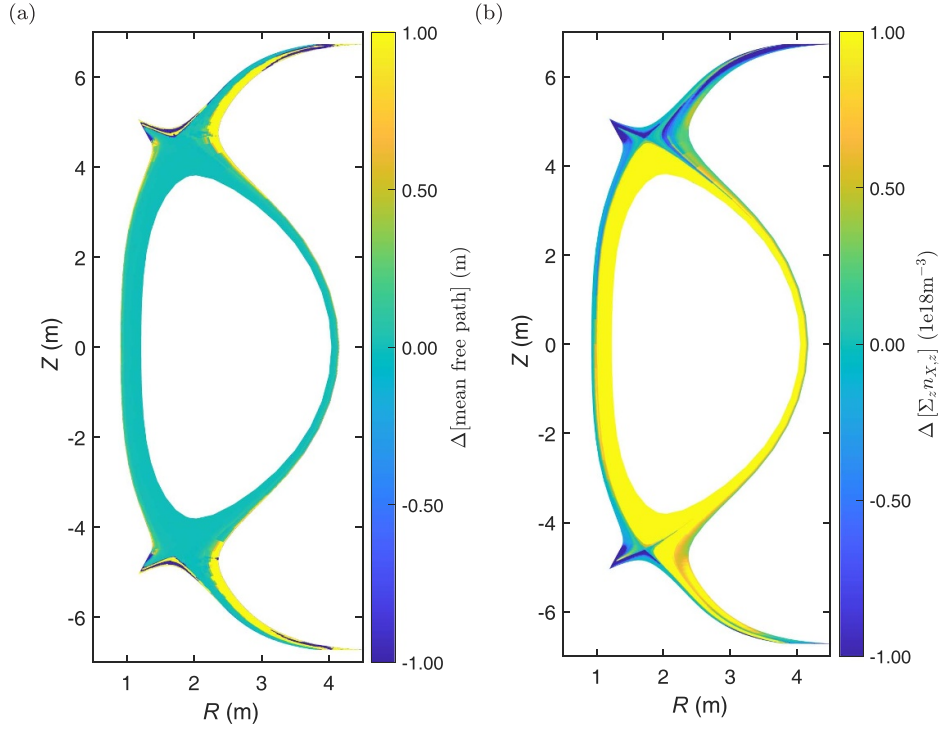
Figure 11. (Left) Difference between neutral neon and argon mean free paths (positive values indicate longer neon mean free path) and (right) difference in total charged impurity density distributions in the connected double null cases with each D puff 4×10^{23} and outer PFR puff of Ne at 3×10^{21}, and inner SOL and outer Ar puffs of 1×10^{21} and 5×10^{21}, respectively.

can travel much more effectively through the outer leg, especially near the separatrix. In figure 11 we show the difference in the total charged impurity density distributions between the cases with each D puff 4×10^{23} and outer PFR puff of Ne at 3×10^{21}, and inner SOL and outer Ar puffs of 1×10^{21} and 5×10^{21}. The strong increase in core neon density with neon seeding is clear, neon does not accumulate in the main chamber SOLs. The source of the up-down power asymmetry noted above is reflected in the up-down asymmetry of impurity content in the outer divertor legs.

Analyzing the parallel force balance, we find that friction dominates the force on the Ne^{1+} around its ionization location in the outer divertor leg, and the impurity is pushed upstream from its ionization location in the outer leg again, but the dominant component is from the total ion-ion friction and is smaller in magnitude than seen in the argon seeding case (figure not shown). The parallel force on the Ne^{1+} in the inner divertor is again very weak, with contributions from friction, near the separatrix, and neutral interactions, with a broader profile. Upstream we find peaked impurity density profiles in the SOL, and radially inward fluxes of states around Ne^{7+}, see figure 12, which are stronger than those in the argon seeded cases (figure 5), lead to the final upstream impurity distributions.

In figure 13 we show the compression of neon and deuterium, as well as the enrichment of neon, as a function of gas puff ratio. The inner divertor is shown on the left panel, and the outer on the right. Again there is weak variation in D compression over the scan, and the trend in neon enrichment follows the neon compression. The outer target shows neon

enrichment weaker than that of argon in figure 3, note the different gas puff range. The inner target again shows negligible enrichment.

3.3. Radiation efficiency

The impurity seeding affects the SOL temperature distribution, but if the impurity is very well localized in the cool divertor, we may expect the net impurity radiation to be lower. Therefore we consider here the variation in radiation efficiency of the impurities as a function of their enrichment. We take the radiation efficiency, per plasma grid cell, as the ratio of the impurity radiation density to the denominator formed by the total density of charged impurity states multiplied by the electron density. To give the radiation efficiency in the outer SOL, this ratio is volume averaged (as defined at the start of section 3) over the entire outer SOL. The analogous definition is used for the inner SOL impurity radiation efficiency.

The enrichment of argon and neon are compared directly for the inner and outer divertors in the upper row (left and right panels respectively) of figure 14. The radiation efficiencies are compared in the lower row. The radiation efficiency in the outer divertors is fairly constant with enrichment, showing no strong reduction in efficiency as the divertor is cooling, over the range simulated. The radiation efficiency in the inner divertor, which had typically low impurity content, is increased to around that of the outer divertor with the introduction of direct seeding. The stronger (roughly doubled) radiation efficiency of argon than neon is in agreement with experimental observations, where the efficiency, compared to that of deuterium,
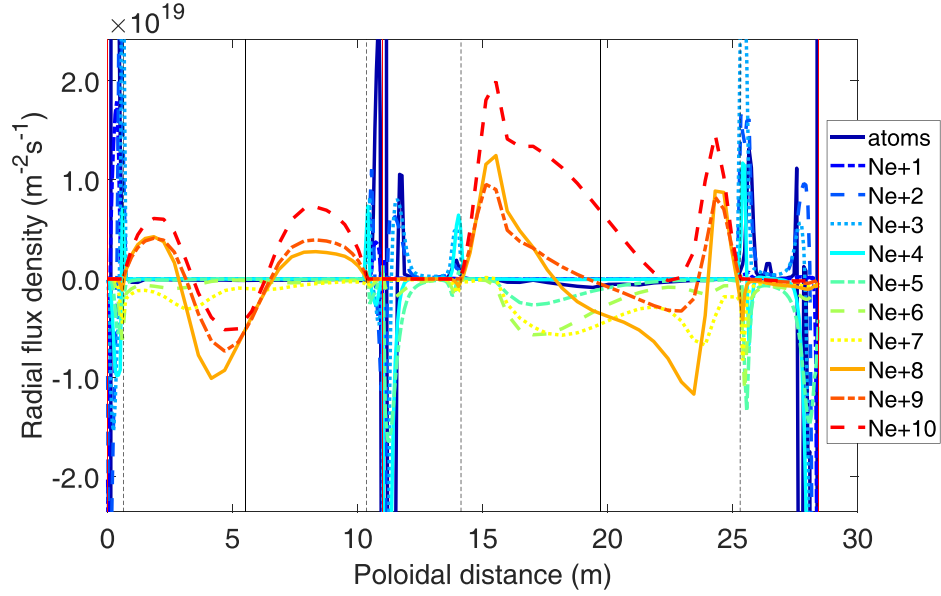
Figure 12. Radial fluxes of Ne charge states across the separatrix, negative inwards, as a function of poloidal distance along the separatrix from the inner target (0 m). Vertical solid line show targets and midplanes, vertical dashed lines show X-point locations. The case is connected double null with both D puffs 4×10^{23} and only outer PFR Ne puff at 3×10^{21}.
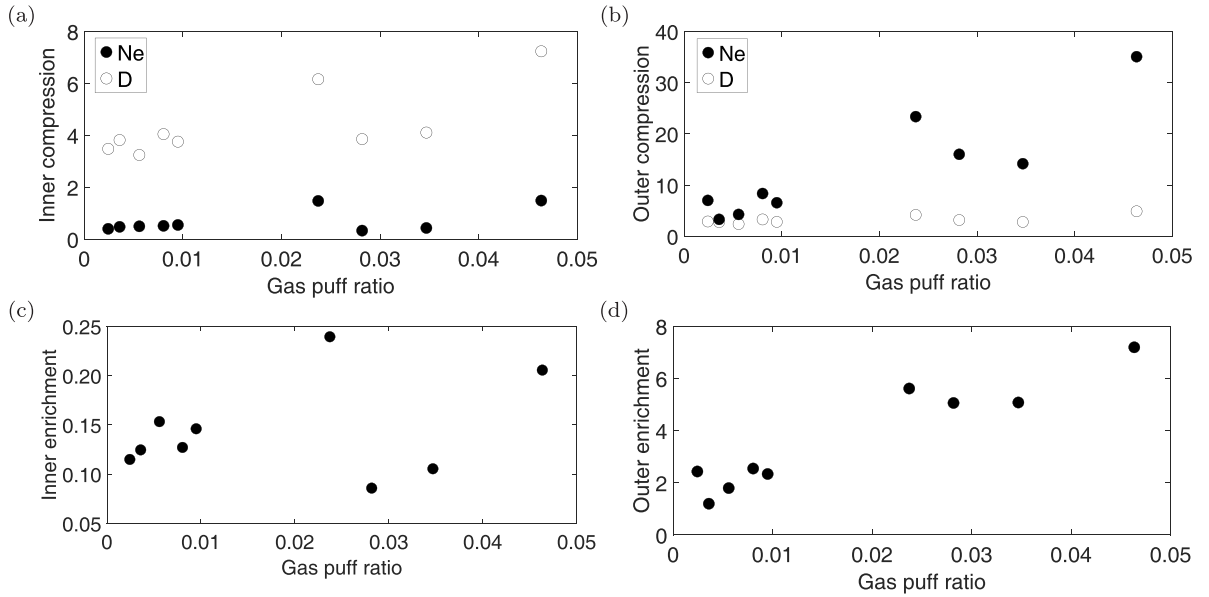

Figure 13. (Top) Neon (solid markers) and deuterium (open markers) compression and (lower) neon enrichment as a function of gas puff ratio for lower inner (left) and outer (right) divertor legs.
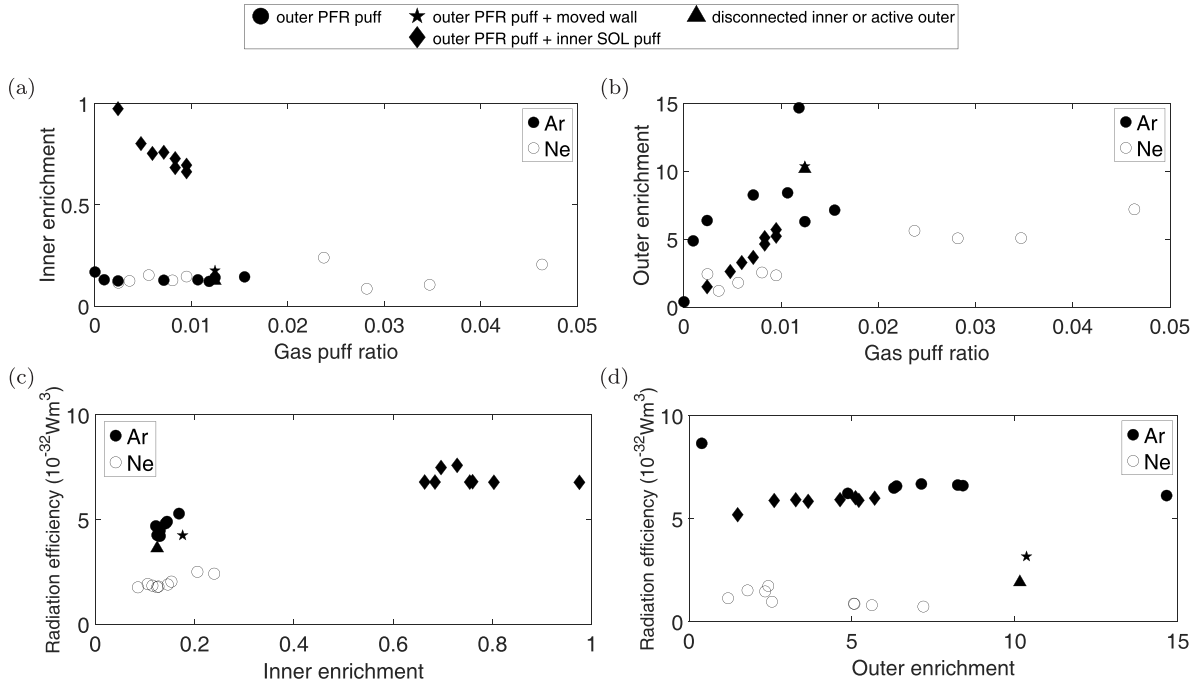
Figure 14. Comparison of argon (solid markers) and neon (open markers) enrichment (top row) and radiation efficiency (lower) as a function of gas puff ratio. Argon plot markers as defined in figure 3.

was used as a fit parameter to model the detachment state [51, 52]. This suggests that neon would be a poor choice for divertor protection in the scenario considered, even if changes to the baffling configuration could be used to reduce its penetration upstream. The weaker outer radiation efficiency in the disconnected equilibrium, when averaging over the whole SOL, results from the low temperature and high impurity density around the inactive lower divertor.

4. Discussion

We have used SOLPS-ITER to study the enrichment of impurities seeded in the divertor to promote detachment: we focused on high power connected double-null ST geometry, with an extended well-baffled outer leg, but a short, weakly baffled, inner leg. The pumping speed and deuterium puffing rates used were high, and must likely be lowered for compatibility with fuel cycle requirements. The vertical inner target generated partially detached solutions unless impurity was seeded directly to the inner target. The input power was fixed to 100 MW, and the range of impurity seeding produced up to 10 MW of radiation losses from the closed field line region.

Argon seeding from the outer PFR reduced the outer target temperature to near 5 eV or less, with the ionization location remaining close to the target. The argon showed good compression and enrichment, with the impurity concentration on the last closed flux surface remaining below 1%, the level at which the impurity may be expected to affect performance of the main core plasma. The trends suggest there may be enough flexibility to handle the higher outboard power load expected when ballooned transport is accounted for [8], but that will be studied in detail with updated machine designs. Weaker enrichment was seen in the outer target with neon seeding, and to produce similar levels of detachment required higher gas puff ratios with neon, due to the different radiation efficiencies of neon and argon as a function of temperature, indicating that neon would be a poor choice for divertor protection in this scenario. The higher FIP of neon was reflected in a longer neutral neon mean free path and wider region of ionization to Ne^{1+} along the outer divertor separatrix, which led to the high core neon concentration in the simulation and impurity concentration up to 9% on the last closed flux surface. Whilst the behavior of argon and neon found here is in qualitative agreement with experimental findings [29, 33], impurity screening physics of the closed field line region is not modeled here [53, 54].

The quoted core concentrations should thus be seen as indicating regimes which may be compatible with main plasma performance and of interest for further study.

Argon seeded in the outer PFR was not readily transmitted to the inner divertor in the simulations (as was also seen experimentally on EAST [37]), which thus showed negligible inner target enrichment. Direct seeding of the inner divertor improved the enrichment, though the short open geometry allowed the upstream impurity concentration to increase quickly as the inner divertor detached. The outer divertor enrichment trend was not affected, which encouraged the exploration of alternative divertor concepts to independently improve the power handling of the inner target [50]. The results also suggest that the in-out balance of seeding could be optimized to promote detachment of both divertors.

The location of the deuterium gas puff slots, which can affect the deuterium flow pattern and so the impurity upstream build-up, has been studied in [49]. We note the net throughput of gas in the simulations is high, but we expect it can be scaled down by reducing the pumping speed, without affecting the enrichment results. However, helium must be pumped from the system and how far the pumping can be reduced whilst the helium pumping remains effective is to be determined. Optimization of the outer leg baffling and pumping geometry is ongoing.

The full impact of including drifts on these results remains to be studied. In the detached phase, the temperature profile across the divertor targets is quite flat, indicating that relatively weak drifts may be expected near the target. There is a stronger radial temperature profile further up the outer leg, which will create stronger drift effects, and affect detachment onset and access. The latter is out of scope of study for this early design phase geometry. The typical drift effect [55] may generate a flow directed towards the target in the outer SOL, and a flow through the PFR to the inner divertor, which may be beneficial for the inner target. However drifts typically produce up-down asymmetric flows and density redistribution. As the main ion flows in the connected double-null cases without drifts simulated here are very weak, a significant change in the balance of flows may be expected with drifts. Initial indications from fixed impurity fraction simulations with drifts are that the high power connected double null scenario considered had an atypical asymmetry, which is the subject of further investigation [43]. Retaining the deep baffling of the outer legs, allowing a region of strong radiation which can affect the flow patterns, may help to maintain impurity compression.

Acknowledgments

Appendix A. EIRENE reaction list

The reactions included in the simulations through EIRENE are given in table A1.

Table A1. Included EIRENE reactions: EL elastic collision, EI electron impact, CX charge exchange, DS dissociation, RC recombination.

Main ion				
1	AMMONX	H.2	R-H-H	EL
2	AMMONX	H.2	R-H-H2	EL
3	AMJUEL	H.4	2.1.5	EI
4	AMJUEL	H.10	2.1.5	EI
5	HYDHEL	H.1	3.1.8	CX
5	HYDHEL	H.3	3.1.8	CX
7	AMMONX	H.2	R-H2-H	EL
8	AMMONX	H.2	R-H2-H2	EL
9	AMJUEL	H.4	2.2.9	EI
10	AMJUEL	H.4	2.2.5 g	DS
11	AMJUEL	H.4	2.2.10	DS
12	AMJUEL	H.0	0.3 T	EL
12	AMJUEL	H.1	0.3 T	EL
12	AMJUEL	H.3	0.3 T	EL
13	AMJUEL	H.2	3.2.3	CX
14	AMJUEL	H.4	2.2.12	DS
15	AMJUEL	H.4	2.2.11	EI
16	AMJUEL	H.4	2.2.14	DS
17	AMJUEL	H.8	2.2.14	DS
18	AMJUEL	H.4	2.1.8	RC
19	AMJUEL	H.10	2.1.8	RC
Argon				
6	AMJUEL	H.2	2.18B0	EI
20	ADAS	H.4	acd89	RC
21	ADAS	H.10	prb89	RC
Neon				
6	AMJUEL	H.2	2.10B0	EI
20	ADAS	H.4	acd96	RC
21	ADAS	H.10	prb96	RC

Appendix B. Compression up-down symmetry

The figures in the main text show the inner and outer compression values averaged over the upper and lower divertor legs. The argon compression evaluated for the individual legs is shown for the main argon scan cases in figure B1, to demonstrate the degree of up-down asymmetry and motivate the averaging used—compare to figures 3(*a*) and (*b*). The up-down
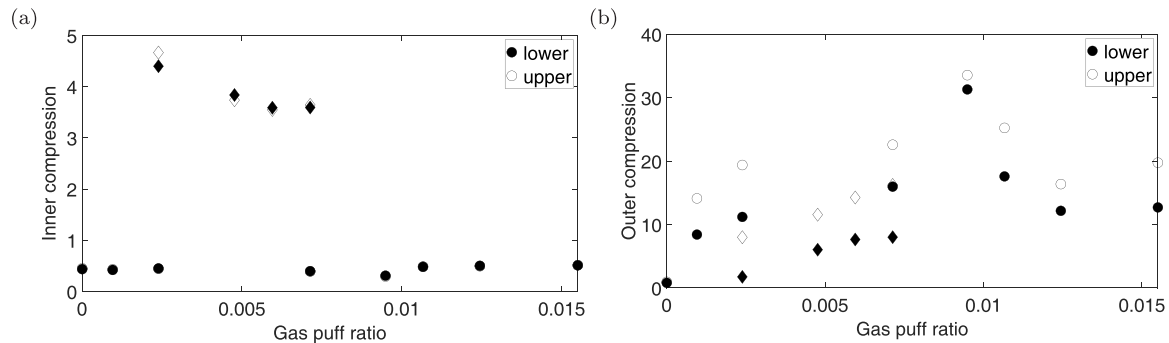
Figure B1. Argon compression as a function of gas puff ratio for inner (left) and outer (right) divertor legs. Lower and upper divertor leg values are shown as solid and open markers, respectively. Marker shape is as in figure 3: cases with only outer PFR Ar puff are shown as circles, and cases with both inner and outer Ar puff are shown as diamonds.

asymmetry in the simulation of the disconnected double-null, and in the high neon content cases, are discussed in the main text.

ORCID iDs

S.L. Newton ![ORCID] 0009-0006-9052-2401
R.T. Osawa ![ORCID] 0000-0002-8152-2323
S.S. Henderson ![ORCID] 0000-0002-8886-1256
O. Myatra ![ORCID] 0000-0002-1469-2429

References

[1] Loarte A. and Neu R. 2017 *Fusion Eng. Des.* **122** 256–73
[2] Eich T. *et al* 2013 *Nucl. Fusion* **53** 093031
[3] Pitcher C.S. and Stangeby P.C. 1997 *Plasma Phys. Control. Fusion* **39** 779–930
[4] Kirk A. *et al* 2004 *Plasma Phys. Control. Fusion* **46** 551
[5] De Temmerman G., Delchambre E., Dowling J., Kirk A., Lisgo S. and Tamain P. 2010 *Plasma Phys. Control. Fusion* **52** 095005
[6] De Temmerman G., Kirk A., Nardon E., Tamain P. and The MAST Team 2011 *J. Nucl. Mater.* **415** S383–6
[7] Brunner D., Kuang A.Q., LaBombard B. and Terry J.L. 2018 *Nucl. Fusion* **58** 076010
[8] Osawa R.T., Moulton D., Newton S.L., Henderson S.S., Lipschultz B. and Hudoba A. 2023 *Nucl. Fusion* **63** 076032
[9] Reimerdes H. *et al* 2020 *Nucl. Fusion* **60** 066030
[10] Fishpool G., Canik J., Cunningham G., Harrison J., Katramados I., Kirk A., Kovari M., Meyer H., Scannell R. and the MAST-upgrade Team 2013 *J. Nucl. Mater.* **438** S356–9
[11] Stangeby P.C. and Leonard A.W. 2011 *Nucl. Fusion* **51** 063001
[12] Aho-Mantila L. *et al* 2021 *Nucl. Mater. Energy* **26** 100886
[13] Lipschultz B., Parra F.I. and Hutchinson I.H. 2016 *Nucl. Fusion* **56** 056007
[14] Kallenbach A. *et al* 2013 *Plasma Phys. Control. Fusion* **55** 124041
[15] Neuhauser J. *et al* 1995 *Plasma Phys. Control. Fusion* **37** A37–A51
[16] Schaffer M.J., Wade M.R., Maingi R., Monier-Garbet P., West W.P., Whyte D.G., Wood R.D. and Mahdavi M.A. 1997 *J. Nucl. Mater.* **241–243** 585–9
[17] Reimold F., Wischmeier M., Bernert M., Potzel S., Kallenbach A., Müller W., Sieglin B., Stroth U. and the ASDEX Upgrade Team 2015 *Nucl. Fusion* **55** 033004
[18] Reinke M.L. 2017 *Nucl. Fusion* **57** 034004
[19] Effenberg F. *et al* 2019 *Nucl. Fusion* **59** 106020
[20] Tanaka H. *et al* 2017 *Nucl. Mater. Energy* **12** 241–6
[21] Meng L.Y. *et al* 2022 *Nucl. Fusion* **62** 086027
[22] Février O. *et al* 2021 *Nucl. Mater. Energy* **27** 100977
[23] Casali L., Osborne T.H., Grierson B.A., McLean A.G., Meier E.T., Ren J., Shafer M.W., Wang H. and Watkins J.G. 2020 *Phys. Plasmas* **27** 062506
[24] Lomanowski B. *et al* 2019 *Nucl. Mater. Energy* **20** 100676
[25] Senichenkov I.Y., Kaveeva E.G., Sytova E.A., Rozhansky V.A., Voskoboynikov S.P., Veselova I.Y., Coster D.P., Bonnin X., Reimold F. and the ASDEX-Upgrade Team 2019 *Plasma Phys. Control. Fusion* **61** 045013
[26] Eldon D. , Wang H.Q., Wang L., Ding S., Garofalo A.M., Gong X.Z., McLean A.G., Scotti F., Watkins J.G. and Weisberg D. 2023 *Nucl. Mater. Energy* **34** 101332
[27] Goetz J.A., Lipschultz B., Pitcher C.S., Terry J.L., Bonoli P.T., Rice J.E. and Wukitch S.J. 1999 *J. Nucl. Mater.* **266** 354–9
[28] Petrie T.W. *et al* 2007 *J. Nucl. Mater.* **363–5** 416–20
[29] Hitzler F., Wischmeier M., Reimold F., Coster D.P. and the ASDEX Upgrade Team 2020 *Plasma Phys. Control. Fusion* **62** 085013
[30] Casali L., Eldon D., Boedo J.A., Leonard T. and Covele B. 2020 *Nucl. Fusion* **60** 076011
[31] Moulton D., Stangeby P.C., Bonnin X. and Pitts R.A. 2021 *Nucl. Fusion* **61** 046029
[32] Zito A. *et al* 2023 *Nucl. Fusion* **63** 096027
[33] Kallenbach A. *et al* 2021 *Nucl. Fusion* **61** 016002
[34] Vekshina E., Korzueva V., Rozhansky V., Senichenkov I., Kaveeva E., Veselova I., Coster D. and Subba F. 2022 *Contrib. Plasma Phys.* **62** e202100176
[35] McCracken G.M., Bombarda F., Graf M., Goetz J.A., Jablonski D., Kurz C., Labombard B., Lipschultz B., Rice J. and Welch B. 1995 *J. Nucl. Mater.* **220–222** 264–8
[36] Casali L., Eldon D., McLean A., Osborne T., Leonard A., Grierson B. and Ren J. 2022 *Nucl. Fusion* **62** 026021
[37] Li K. *et al* 2021 *Nucl. Fusion* **61** 066013
[38] Wiesen S. *et al* 2015 *J. Nucl. Mater.* **463** 480–4
[39] Bonnin X., Dekeyser W., Pitts R., Coster D., Voskoboynikov S., Wiesen S. and Voskoboynikov S. 2016 *Plasma Fusion Res.* **11** 1403102
[40] Reiter D., Baelmans M. and Börner P. 2005 *Fusion Sci. Technol.* **47** 172–86
[41] Wilson H., Chapman I., Denton T., Morris W., Patel B., Voss G., Waldon C. and the STEP Team 2020 *Step-On the*

Pathway to Fusion Commercialisation (*Commercialising Fusion Energy)* (IoP Publishing) (https://doi.org/10.1088/978-0-7503-2719-0)

[42] Meyer H. 2023 The plasma scenarios for the Spherical Tokamak for Energy Production (STEP) and their technical implications *Preprint: 2023 IAEA Fusion Energy Conf., London [TH-C P/6 2148]* (available at: https://conferences.iaea.org/event/316/)

[43] Karhunen J., Järvinen A., Henderson S.S., Moulton D., Newton S. and Osawa R.T. 2023 First SOLPS-ITER predictions of the impact of cross-field drifts on divertor and scrape-off layer conditions in double-null configuration of STEP *Preprint: 2023 IAEA Fusion Energy Conf., London [TH-D P/7 2067]*

[44] Chang C.S. , Ku S., Hager R., Churchill R.M., Hughes J., Köchl F., Loarte A., Parail V. and Pitts R.A. 2021 *Phys. Plasmas* **28** 022501

[45] Havlíčková E. *et al* 2015 *Plasma Phys. Control. Fusion* **57** 115001

[46] Loarte A. 2001 *Plasma Phys. Control. Fusion* **43** R183–224

[47] Kirschner A. *et al* 2023 *Nucl. Fusion* **63** 126055

[48] Stangeby P.C. 2000 *The Plasma Boundary of Magnetic Fusion Devices* (IoP Publishing)

[49] Osawa R.T., Newton S.L., Moulton D., Henderson S.S., Hudoba A. and Badicel V. 2023 SOLPS-ITER assessment of the impact of fuelling and seeding puff locations on divertor impurity retention in STEP *Preprint: 2023 IAEA Fusion Energy Conf., London [TH-D P/6 2363]* (available at: https://conferences.iaea.org/event/316/)

[50] Hudoba A., Newton S., Voss G., Cunningham G. and Henderson S. 2023 *Nucl. Mater. Energy* **35** 101410

[51] Kallenbach A., Bernert M., Dux R., Reimold F., Wischmeier M. and ASDEX Upgrade Team 2016 *Plasma Phys. Control. Fusion* **58** 045013

[52] Henderson S.S. *et al* 2023 *Nucl. Fusion* **63** 086024

[53] Angioni C. 2021 *Plasma Phys. Control. Fusion* **63** 073001

[54] Field A.R. *et al* 2023 *Nucl. Fusion* **63** 016028

[55] Wensing M., Loizu J., Reimerdes H., Duval B.P., Wischmeier M. and the TCV team 2020 *Nucl. Fusion* **60** 054005